RESEARCH ARTICLE

Surface modulated Fe doping of β-Ni(OH)₂ nanosheets for highly promoted oxygen evolution electrocatalysis

Shuisheng Hu[1,2] | **Yong Li**[1] | **Daekyu Kim**[1] | **Mengjie Liu**[1] |
Lawrence Yoon Suk Lee[1,3] | **Kwok-Yin Wong**[1]

[1]Department of Applied Biology and Chemical Technology and the State Key Laboratory of Chemical Biology and Drug Discovery, The Hong Kong Polytechnic University, Hong Kong SAR, China

[2]Key Laboratory of Prevention and Treatment of Cardiovascular and Cerebrovascular Diseases, Ministry of Education, Gannan Medical University, Ganzhou, China

[3]Research Institute for Smart Energy, The Hong Kong Polytechnic University, Hong Kong SAR, China

Correspondence
Lawrence Yoon Suk Lee and Kwok-Yin Wong, Department of Applied Biology and Chemical Technology and the State Key Laboratory of Chemical Biology and Drug Discovery, The Hong Kong Polytechnic University, Hung Hom, Kowloon, Hong Kong SAR, China.
Email: lawrence.ys.lee@polyu.edu.hk and kwok-yin.wong@polyu.edu.hk

Abstract
Active yet low-cost electrocatalysts for water oxidation are crucial for the development of hydrogen energy economy. The Fe doping into Ni(OH)₂ dramatically enhances catalytic activity toward oxygen evolution reaction (OER) but fabricating Ni(OH)₂ of high Fe loading is still challenging. Herein, we report a one-pot strategy to prepare disordered β-Ni(OH)₂ nanosheets with a high Fe doping level (9.9 at%, D-Fe-Ni(OH)₂). By engaging 1,4-phenylenediphosphonic acid (BDPA), Fe_xBDPA_y precursors are in situ generated in a growth solution containing Fe^{3+} ions, which decrease the reaction kinetics of Ni^{2+} and Fe^{3+} ions at the surface of Ni foam. This prevents the deconstructive hydrolysis by Fe^{3+} ions and enables a high Fe-doping in D-Fe-Ni(OH)₂. The as-prepared D-Fe-Ni(OH)₂ affords 10 mA cm^{-2} at an ultralow OER overpotential of 194 mV in alkaline media. This work offers a promising strategy of engaging organic ligands to achieve high-doping levels for the construction of efficient electrocatalysts.

KEYWORDS
electrocatalysis, high Fe doping, in situ Raman spectroscopy, nickel–iron hydroxide, oxygen evolution reaction

1 | INTRODUCTION

Hydrogen is an important feedstock for the chemical industry and is widely believed to become a next-generation high-density energy carrier.[1] Electrocatalytic water splitting, which is comprised of oxygen and hydrogen evolution reactions (OER and HER), driven by renewable electricity can offer a sustainable pathway

toward large-scale hydrogen production.[2] However, the multiple proton-coupled electron transfer process involved in OER is sluggish and thus mainly responsible for the high overpotential of electrochemical water splitting. Active and cost-effective OER catalysts based on non-precious metals are highly desirable to reduce the overpotential and facilitate the overall water splitting process.

Recently, layered double hydroxides (LDHs) have attracted wide attention thanks to their high OER activity

---

Shuisheng Hu and Yong Li contributed equally to this study.

under alkaline conditions.[3] In particular, nickel-iron LDHs (NiFe-LDHs) have demonstrated impressive OER activities that largely surpass that of both $Ni(OH)_2$ and $Fe(OH)_3$.[4,5] Such enhanced OER activity of NiFe-LDHs arises from the following three aspects: (1) The insertion of Fe into an n-type semiconductor NiOOH can promote its low specific conductance (σ) of 0.1 to 3.5–6.5 mS cm^{-2}. The increased conductivity minimizes the potential drop and charge transfer resistance, leading to enhanced catalytic activity; (2) Partial charge transfer between Ni and Fe increases the number of exposed active sites (Ni^{4+}) at the corner and edge sites, which are responsible for the adsorption and desorption of hydroxo- and oxo-intermediates; and (3) The combining of two atoms located on the opposite side of the Volcano plot can optimize the bond strengths of metal–OH intermediates, neither too strong nor too weak.

The cooperative interaction between Ni and Fe toward OER catalysis was also realized by doping Fe into $Ni(OH)_2$, which offers a more tunable and simpler system compared with NiFe-LDHs.[6–9] Recently, Kou et al. reported that a direct reaction of $Fe(NO_3)_3$ with Ni foam ($Ni^0 + NO_3^- + H^+ \rightarrow Ni^{2+} + NO_2^- + OH^-$) could produce ultrathin Fe-doped $Ni(OH)_2$ nanosheets that showed further boosted OER activities with a low (0.54 at %) Fe doping.[10] They claimed that the OER performance deteriorated with further increased Fe doping due to the detachment of $Ni(OH)_2$ nanosheets from the Ni foam at a high Fe^{3+} concentration (~1.5 mM). At high Fe^{3+} concentrations, the strong hydrolysis of Fe^{3+} ($Fe^{3+} + 3H_2O \rightarrow Fe(OH)_3 + 3H^+$) substantially increases the local concentration of protons, resulting in the destabilization of hydroxides as well as the hindrance of their formation.[11] Thus, for the investigation of optimal catalytic activity of highly Fe-doped $Ni(OH)_2$, the prevention of Fe^{3+}-induced hydrolysis is crucial.

Metal–organic frameworks (MOFs) have recently received intensive attention from various research fields as a versatile material system that can be easily and rapidly prepared by simple mixing of metal salts and various organic ligands.[12,13] The spontaneous coordination of metal ions with organic ligands yields a stable yet dynamic MOF structure that slowly releases metal species under alkaline conditions.[14] Inspired by this, we herein report the synthesis of disordered β-$Ni(OH)_2$ nanosheets of high Fe doping (D-Fe-$Ni(OH)_2$) by controlling the release of Fe^{3+} ions with an organic molecule, 1,4-phenylenediphosphonic acid (BDPA). The strong coordination between Fe^{3+} and BDPA rapidly forms Fe_xBDPA_y precursors that effectively trap the Ni^{2+} ions released from the surface of Ni foam, regulating the transfer kinetics of dissociative Fe^{3+} ions to the surface during the formation of D-Fe-$Ni(OH)_2$. This allows the use of high $Fe(NO_3)_3$ concentrations of up to 75 mM to prepare highly Fe-doped D-Fe-$Ni(OH)_2$ with a disordered structure. The as-synthesized D-Fe-$Ni(OH)_2$ exhibits extraordinary OER catalytic activity as manifested by an ultralow overpotential of 194 mV to achieve 10 mA cm^{-2} in 1.0 M KOH, as well as outstanding stability.

2 | RESULTS AND DISCUSSION

2.1 | Characterization of D-Fe-Ni(OH)₂

Figure 1A illustrates the synthetic procedure of disordered Fe-doped β-$Ni(OH)_2$ nanosheets (D-Fe-$Ni(OH)_2$) on Ni foam. Briefly, a piece of Ni foam (1.7×1.7 cm^2) was immersed in a 10 ml growth solution containing 1,4-phenylenediphosphonic acid (BDPA, 0.25 mmol) and $Fe(NO_3)_3$ (0.75 mmol), and D-Fe-$Ni(OH)_2$ was formed by hydrothermal treatment at 180°C for 12 h. When BDPA and $Fe(NO_3)_3$ are mixed in a growth solution, an instant color change from transparent to translucent milky color is observed (Figure S1A–C). Considering that BDPA is stable in 3 wt% HNO_3 (Figure S1D), such a color change indicates a fast interaction between BDPA and Fe^{3+} to form stable Fe_xBDPA_y precursors. The growth solution has a low pH value of 1.06, which is attributed to the release of protons from BDPA and a potential hydrolysis reaction of Fe^{3+} species ($Fe^{3+} + 3H_2O \rightarrow Fe(OH)_3 + 3H^+$). Since the Ni foam serves as both the support and Ni source to form $Ni(OH)_2$ nanosheets, a low pH value is beneficial for the release of Ni^{2+} species to grow $Ni(OH)_2$.

The as-prepared D-Fe-$Ni(OH)_2$ is dominated by β-$Ni(OH)_2$ phase as indicated by the powder X-ray diffraction (XRD) pattern (JCPDS No. 14-0117, Figure 1B).[15] Scanning electron microscopic (SEM) images in Figure 1C disclose the 3D nanostructure of D-Fe-$Ni(OH)_2$, where tiny nanosheets (length = 1 μm) are cross-linked to form a moss lawn-like structure over the entire surface of Ni foam. The individual flake of the nanostructure shows characteristic nanosheet features of a creased and wrinkled surface under transmission electron microscopy (TEM, Figure 2A). A high-resolution TEM (HR-TEM, Figure 2B) image further reveals the areas with a lattice spacing of 0.233 nm, which corresponds to the (101) plane of $Ni(OH)_2$,[16] while the long-range disorganized interplanar spacings indicate the disordered nature of D-Fe-$Ni(OH)_2$. Energy dispersive X-ray (EDX) elemental mapping images (Figure 2C) confirm that Ni, Fe, and O elements are well-distributed on the D-Fe-$Ni(OH)_2$ nanosheet while the P element is negligible. Inductively coupled plasma optical emission spectroscopy (ICP-OES) indicates that the amount of Fe atoms doped in the β-Ni

FIGURE 1 (A) Schematic illustration of the fabrication route for D-Fe-Ni(OH)$_2$. (B) X-ray diffraction (XRD) pattern, (C) Low-resolution scanning electron microscopic (SEM) image, and inset in (C) is an enlarged SEM image of D-Fe-Ni(OH)$_2$. Red circle in the inset of (C) indicates a nanobelt structure
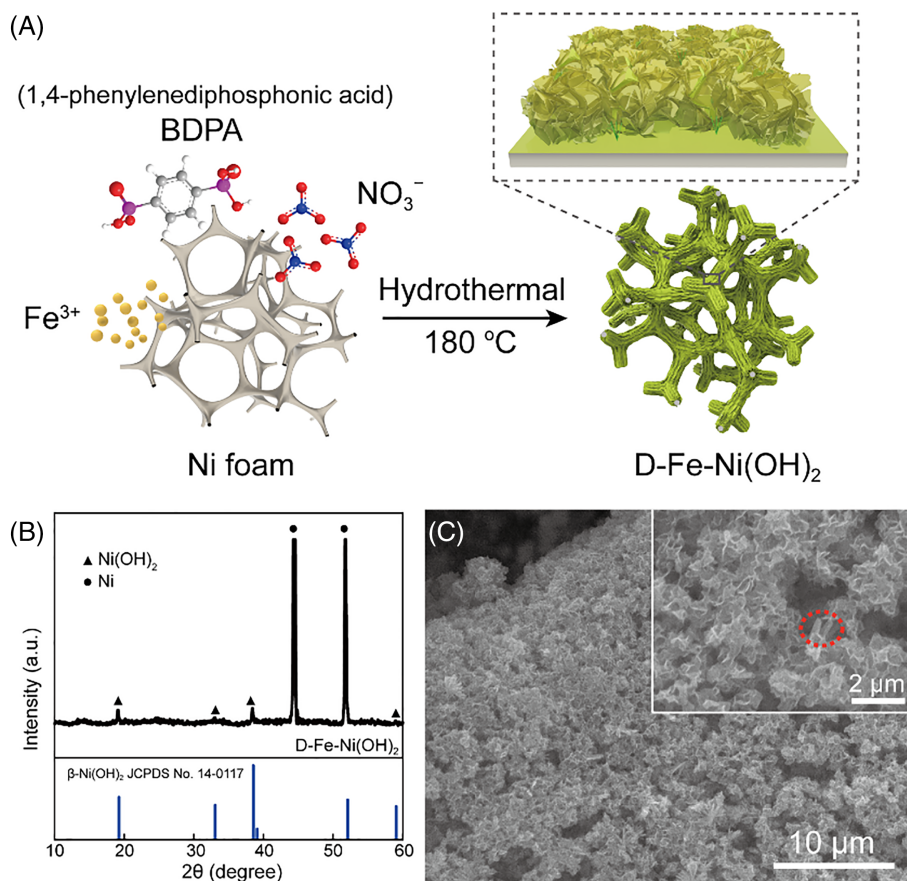
(OH)$_2$ is ca. 9.9 at% (Table S1). It is worth noting that both SEM and TEM images show distinct nanobelt structures surrounded by Fe-doped β-Ni(OH)$_2$ nanosheets (inset in Figures 1C and S2). These nanobelts are mostly amorphous and dominated by Ni, O, and P elements, which are formed as the byproducts of Ni$_z$BDPA$_y$. To gain better insights into the structure of D-Fe-Ni(OH)$_2$, aberration-corrected scanning TEM (STEM), high-angle annular dark field-STEM (HAADF-STEM), and electron energy loss spectroscopy (EELS) were employed. Bright-field STEM image in Figure 3A confirms the disordered crystal structure of D-Fe-Ni(OH)$_2$ and a lattice spacing of 0.233 nm from the (101) plane of Ni(OH)$_2$. From the HAADF-STEM image of D-Fe-Ni(OH)$_2$ (Figure 3B), it is difficult to distinguish Ni and Fe atoms due to their similar contrast. However, STEM-EDX mapping images in Figure 3C verify that Ni and Fe atoms are atomically dispersed in D-Fe-Ni(OH)$_2$. Notably, a number of micropores are observed from the HAADF-STEM image, which are believed to serve as an effective mass transport channel for improved catalytic activity. The EELS spectrum in Figure 3D shows the oxygen K edge at 542.9 eV arising from the oxygen sites octahedrally coordinated to Fe and Ni cations.[17] The Fe and Ni EELS spectra of D-Fe-Ni(OH)$_2$ display Fe L$_3$ and L$_2$ peaks at 714.4 and 725.8 eV and Ni L$_3$ and L$_2$ peaks at 860.0 and 877.5 eV, respectively (Figure 3E,F), confirming the existence of Ni—O, Fe—O, or even Ni—O—Fe bonds in D-Fe-Ni(OH)$_2$.[17,18]

X-ray photoelectron spectroscopy (XPS) was used to study the chemical composition and surface electronic states of D-Fe-Ni(OH)$_2$. The survey spectrum verifies the existence of Fe, Ni, O, and P elements in D-Fe-Ni(OH)$_2$ (Figure S3A). The high-resolution Fe 2p spectrum in Figure S3B is deconvoluted to reveal two pairs of spin–orbit splits (Fe 2p$_{3/2}$ and Fe 2p$_{1/2}$) and a broad satellite peak. The fitted Fe 2p$_{3/2}$ and Fe 2p$_{1/2}$ peaks at 711.6 and 723.5 eV, respectively, are assigned to Fe^{2+} species, while those at higher binding energies (714.2 and 726.2 eV) are attributed to Fe^{3+} species.[19,20] The shakeup satellite peak at 718.3 eV further confirms the doping of Fe^{3+} species.[21] Similarly, in the Ni 2p region (Figure S3C), two pairs of Ni 2p$_{3/2}$ (855.3 and 856.6 eV) and Ni 2p$_{1/2}$ peaks (872.8 and 874.4 eV) are assigned to Ni^{2+} and Ni^{3+} species, respectively, while two strong shakeup satellite peaks at 861.5 and 879.5 eV are induced by Ni^{2+} species.[22,23] It is worth noting that only one pair of Ni 2p$_{3/2}$ and Ni 2p$_{1/2}$ peaks (855.2 and 872.8 eV, respectively) are recognized in pristine Ni(OH)$_2$ (Figure S4), which suggests partial electron transfer from Ni to Fe in D—Fe—Ni(OH)$_2$. The binding energy difference of 17.5 eV between the two Ni
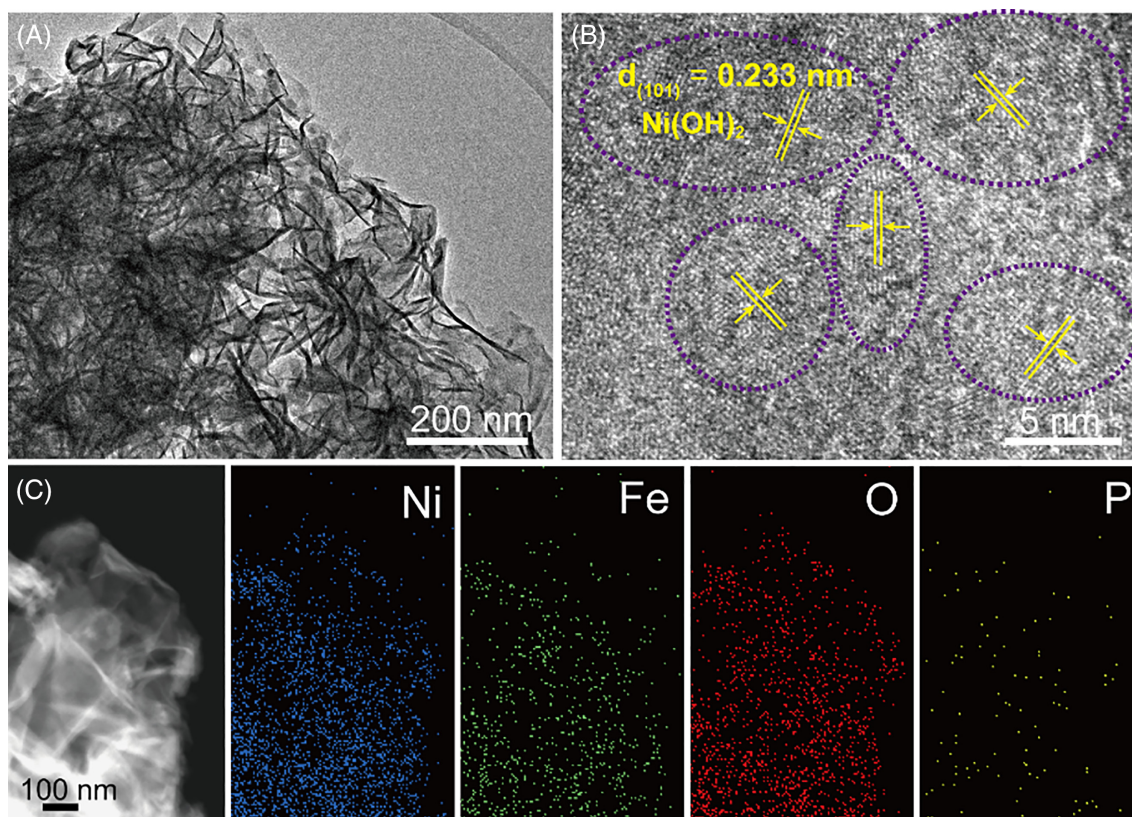
FIGURE 2 (A) Low- and (B) high-resolution transmission electron microscopy (TEM) images, and (C) energy dispersive X-ray (EDX) elemental mapping images of D-Fe-Ni(OH)$_2$

2p peaks indicates that Ni(OH)$_2$ is the dominant phase in D-Fe-Ni(OH)$_2$. The O 1 s spectrum of D—Fe—Ni(OH)$_2$ can be fitted to three peaks (Figure S3D). Two peaks at 530.4 and 531.1 eV correspond to the lattice oxygen from M—O—M and M—OH bonds. Another peak observed at 532.0 eV is ascribed to the adsorbed H$_2$O.[24] Three fitted C 1 s peaks at the binding energies of 284.6, 285.2, and 288.2 eV correspond to the C—C, C—P—O, and C—P=O bonds, respectively (Figure S3E).[25] In addition, a weak P 2p signal can be deconvoluted into two P 2p$_{3/2}$ peaks that are assigned to the characteristic C—P bond in Ni$_z$BDPA$_y$ (132.4 eV) and the P—O bond (133.3 eV, Figure S3F).[26]

2.2 | Formation mechanism of D-Fe-Ni(OH)$_2$

To understand the growth mechanism and the role of BDPA, a set of Fe-doped β-Ni(OH)$_2$ was synthesized using a method previously reported. In the absence of BDPA, Ni foam was treated in the Fe(NO$_3$)$_3$ solution of various concentrations (2.5, 5, 10, and 20 mM) under the same hydrothermal conditions, and denoted as NiFeOH-1 to NiFeOH-4, respectively. All the control samples exhibit similar XRD patterns of β-Ni(OH)$_2$ (Figure S5) with Fe species identified (Figure S6) and thus are confirmed as Fe-doped β-Ni(OH)$_2$. The SEM analyses indicate that NiFeOH-1 and NiFeOH-2 have large nanosheets (length = ~6 μm) fully covering the Ni foam but that NiFeOH-3 with much fewer nanosheets exposes the bare surface of the Ni foam (Figure S7). Moreover, the nanosheets are converted to microspheres in NiFeOH-4, which suggests that β-Ni(OH)$_2$ is unstable in the growth solution of high Fe(NO$_3$)$_3$ concentrations. The use of BDPA, which induces the formation of Fe$_x$BDPA$_y$ precursors in the growth solution, is thus indispensable for the growth of D-Fe-Ni(OH)$_2$ in a highly concentrated Fe(NO$_3$)$_3$.

Considering the strong interaction between Fe^{3+} and BDPA, it is still unclear how the Fe$_x$BDPA$_y$ affects the growth of D=Fe-Ni(OH)$_2$. In another control experiment, the Fe$_x$BDPA$_y$ precursors were isolated from the growth solution by centrifugation and washed with deionized water to remove the uncoordinated Fe^{3+} ions. The XRD and EDX analyses suggest an amorphous nature of Fe$_x$BDPA$_y$ with well-distributed Fe, P, and O elements (Figures S8 and S9). By re-dispersing the Fe$_x$BDPA$_y$ precursors in 1 M HNO$_3$ and using it as the growth solution under the same hydrothermal conditions, Ni(OH)$_2$ nanosheets of ca. 3 μm length can be
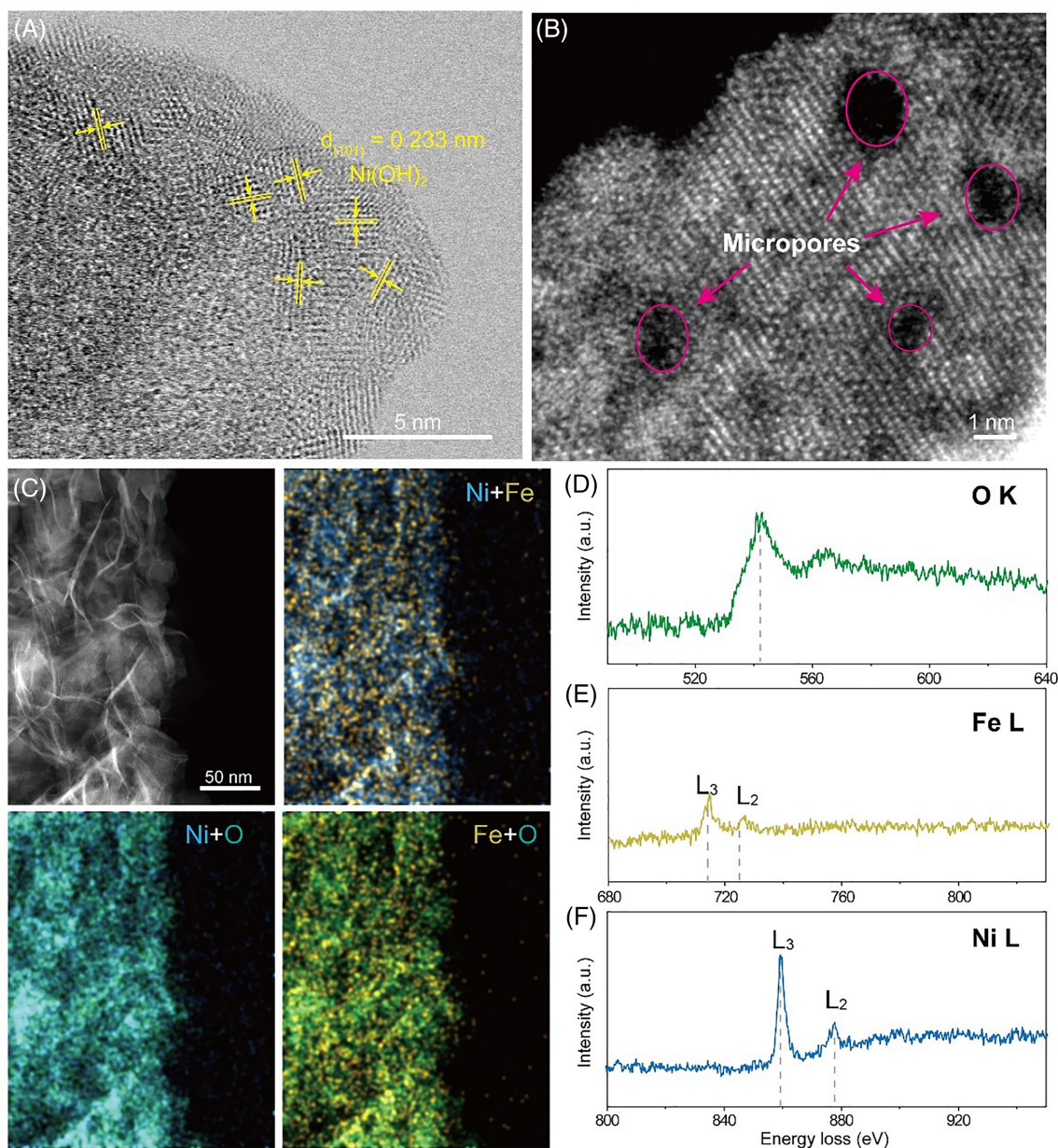
FIGURE 3 (A) Bright-field scanning electron microscopic (SEM), (B) high-angle annular dark field (HAADF)-STEM, and (C) STEM-energy dispersive X-ray (EDX) mapping images of D-Fe-Ni(OH)$_2$. Electron energy loss spectroscopy (EELS) spectra of D-Fe-Ni(OH)$_2$ in (D) O K edge, (E) Fe L edge, and (F) Ni L edge regions

formed on a Ni foam (D-Fe-Ni(OH)$_2$-p, Figures S10 and S11). The Fe$_x$BDPA$_y$ precursors are believed to retain the Ni^{2+} species released from the Ni foam which further reacts with OH$^-$ to grow Ni(OH)$_2$ nanosheets under hydrothermal conditions. ICP-OES estimates the Fe content doped in the Ni(OH)$_2$ is ca. 2.7 at% (Table S1), which indicates that a replacement reaction has taken place between the Fe$_x$BDPA$_y$ precursors and Ni^{2+} (zNi^{2+} + Fe$_x$BDPA$_y$ → Ni$_z$BDPA$_y$ + xFe^{3+}), and the released Fe^{3+} ions are doped to Ni(OH)$_2$. The lower Fe doping level than in D-Fe-Ni(OH)$_2$ (9.9 at%) suggests that the Fe species in the growth solution also contributes in

addition to the Fe$_x$BDPA$_y$ precursors. Meanwhile, the Ni foam that is immersed in a bare HNO$_3$ solution, without the addition of any Fe$_x$BDPA$_y$ precursors, does not form any nanosheet structures by the same hydrothermal reaction (Figure S12). On the other hand, the supernatant of the growth solution also contains 0.448 mmol of Fe^{3+} after the removal of Fe$_x$BDPA$_y$ precursors (Table S1). The same hydrothermal treatment of Ni foam in the supernatant solution, however, cannot grow nanosheets (Figure S13), which can be ascribed to the high concentration of dissociative Fe^{3+} and NO$_3^-$ ions. This is consistent with the previous

result that almost no nanosheets are formed on D-Fe-Ni(OH)$_2$–4.

The Fe$_x$BDPA$_y$ precursors in the growth solution play an essential role in achieving a high Fe doping in the resultant D-Fe-Ni(OH)$_2$. The growth mechanism of D-Fe-Ni(OH)$_2$ is proposed as follows. Owing to the presence of NO$_3^-$ and H$^+$ ions in the growth solution, the Ni^0 atoms on the Ni foam are first oxidized to Ni^{2+} while the H$^+$ ions form OH$^-$ species in the vicinity of the Ni foam (Ni^0 + NO$_3^-$ + H$^+$ → Ni^{2+} + NO$_2^-$ + OH$^-$). Although Ni^{2+} ions might be generated by the reduction of Fe^{3+} and/or H$^+$ (Ni^0 + 2Fe^{3+} → Ni^{2+} + 2Fe^{2+}; Ni^0 + 2H$^+$ → Ni^{2+} + H$_2$), the NO$_3^-$ reduction has a lower Gibbs free energy than the Fe^{3+}/H$^+$ reductions, and the formation of OH$^-$ species confirms that the former reaction dominates during the hydrothermal reaction.[11] The Fe$_x$BDPA$_y$ precursors effectively trap the Ni^{2+} ions released from the Ni foam surface, regulating the transfer kinetics of dissociative Fe^{3+} ions to the surface during the formation of D-Fe-Ni(OH)$_2$. Meanwhile, the Ni$_z$BDPA$_y$ nanobelts are formed due to the partial replacement reaction between Ni^{2+} and Fe$_x$BDPA$_y$.

To verify the growth mechanism of D-Fe-Ni(OH)$_2$, the amount of Fe(NO$_3$)$_3$ was varied from 0 to 0.1, 0.5, and 0.85 mmol in the synthesis of D-Fe-Ni(OH)$_2$ using a fixed amount of BDPA (0.25 mmol), and the corresponding products are named as D-Fe-Ni(OH)$_2$–1 to D-Fe-Ni(OH)$_2$–4, respectively. In the absence of BDPA, flower-like structures of Ni$_z$BDPA$_y$ nanobelts are obtained (D-Fe-Ni(OH)$_2$-1, Figure S14A–C). The D-Fe-Ni(OH)$_2$-2 prepared with 0.1 mmol Fe^{3+} is still dominated by Ni$_z$BDPA$_y$ while a few nanosheets are observed from the surface of the nanobelts due to the prevailing free BDPA molecules (Figure S14D–F). With the addition of 0.5 mmol Fe(NO$_3$)$_3$, most BDPA molecules react with Fe^{3+} to form Fe$_x$BDPA$_y$ precursors, and D-Fe-Ni(OH)$_2$–3 of similar morphology and structure to the D—Fe—Ni(OH)$_2$-p results in a higher Fe doping level (5.2 at%, Figure S14G–I and Table S1). A further increase of Fe(NO$_3$)$_3$ to 0.85 mmol produces almost the same nanosheets as D-Fe-Ni(OH)$_2$ (D-Fe-Ni(OH)$_2$–4, Figure S14J–L), but the Fe doping level is lower (6.7 at%) than D-Fe-Ni(OH)$_2$. The high Fe^{3+} concentration is believed to have caused an accelerated consumption of Ni^0, which would result in the dissolution of the Ni foam. For the growth of D-Fe-Ni(OH)$_2$ at a high Fe doping level, the synergistic interplays among Fe^{3+}, NO$_3^-$, and Fe$_x$BDPA$_y$ precursors of optimized concentrations are important.

2.3 | OER catalysis by D-Fe-Ni(OH)$_2$

The electrocatalytic OER activities of the as-prepared samples were investigated by linear sweep voltammetry (LSV) at a sweeping rate of 0.1 mV s^{-1} in 1.0 M KOH. Figure S15 compares the OER performances of the NiFe-OH samples that were prepared without using BDPA, and NiFe-OH–2 exhibits the best OER activity with a low overpotential (η_{10}) of 214 mV at a current density of 10 mA cm^{-2}, a moderate Tafel slope of 53.8 mV dec^{-1}, and a large active surface area (30.47 mF cm^{-2}). Also, the OER performances of the D-Fe-Ni(OH)$_2$ samples were compared in Figure S16. The η_{10} of D-Fe-FeNi(OH)$_2$, D-Fe-Ni(OH)$_2$–1, D-Fe-Ni(OH)$_2$–2, D-Fe-Ni(OH)$_2$–3, and D-Fe-Ni(OH)$_2$–4 are determined as 194, 336, 291, 224, and 209 mV, respectively, revealing the OER kinetics of the Fe doped Ni(OH)$_2$ nanosheets is faster than that of Ni$_z$BDPA$_y$. An increasing trend in OER activity is observed as the Fe doping level in Ni(OH)$_2$ nanosheets increases.

Figure 4A compares the OER performances of D-Fe-Ni(OH)$_2$, β-Ni(OH)$_2$, NiFeOH-2, and commercial RuO$_2$. The β-Ni(OH)$_2$ nanosheets (length = 5 μm) were prepared based on our previous work[27] and used as a control sample to compare the OER active sites of D-Fe-Ni(OH)$_2$ (Figure S17). The pristine β-Ni(OH)$_2$ shows the lowest OER activity, recording the largest η_{10} of 318 mV. D-Fe-Ni(OH)$_2$ displays the highest OER activity with an impressive η_{10} of 194 mV, outperforming the commercial RuO$_2$ (280 mV) and NiFeOH-2 (214 mV). We attribute the superior OER activity of D-Fe-Ni(OH)$_2$ to the following two aspects: (1) the Fe ions in Ni(OH)$_2$ lattice induce the redistribution of electrons on the Ni atom; and (2) the large amount of Fe triggers a phase transformation from a well-defined crystal structure to an amorphous one, exposing more active sites. The corresponding Tafel plots constructed using the LSV data provide insight into the OER kinetics (Figure 4B). D-Fe-Ni(OH)$_2$ exhibits a Tafel slope of 30.7 mV dec^{-1}, which is much smaller than all other samples compared (NiFeOH-2: 53.8 mV dec^{-1}, RuO$_2$: 51.7 mV dec^{-1}, and β-Ni(OH)$_2$: 51.5 mV dec^{-1}). Such an extremely small value of Tafel slope reflects the superb OER kinetics of D-Fe-Ni(OH)$_2$, which surpasses most Ni(OH)$_2$-based electrocatalysts recently reported (Table S2).

To better understand the high OER performance and identify the active site of D-Fe-Ni(OH)$_2$, electrochemically active surface area (ECSA) was determined by measuring CVs at various scan rates from 5 to 100 mV s^{-1} in 1.0 M KOH.[28] Plotting the difference between anodic and cathodic current densities ($D_j = [j_a - j_c]/2$) at 0.25 V (vs. Hg/HgO electrode) against the scan rate yields a linear relationship, and the slope indicates double-layer capacitance (C_{dl}) that represents the corresponding ECSA (Figure 4C). The larger C_{dl} of D-Fe-Ni(OH)$_2$ (43.17 mF cm^{-2}) than β-Ni(OH)$_2$ (13.53 mF cm^{-2}) and NiFeOH-2

FIGURE 4 (A) Linear sweep voltammetry (LSV) curves and (B) the corresponding Tafel slopes of D-Fe-Ni$(OH)_2$, NiFeOH-2, RuO_2, and β-Ni$(OH)_2$. (C) Double-layer capacitances of D-Fe-Ni$(OH)_2$, NiFeOH-2, and Ni$(OH)_2$. (D) LSVs before and after 500 CV cycles. Inset is the chronoamperometric curve of D-Fe-Ni$(OH)_2$ at 30 mA cm^{-2} for 10 h
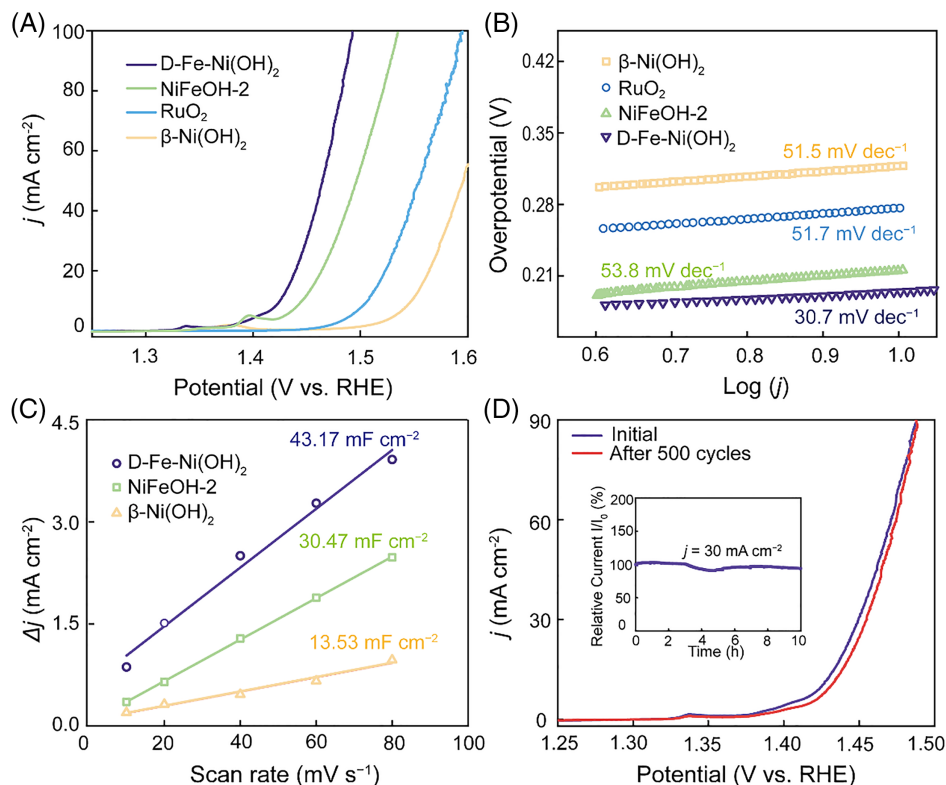
(30.47 mF cm^{-2}) suggests its abundant catalytically active sites on the surface. Electrochemical impedance spectroscopy (EIS) was also performed at a potential of 1.42 V versus RHE to probe the charge transfer properties during the OER process (Figure S18). D-Fe-Ni$(OH)_2$ displays a smaller semicircle in the Nyquist plot compared with NiFeOH-2 and β-Ni$(OH)_2$, which indicates the lowest charge transfer resistance (R_{ct}) and thus improved reaction kinetics leading to superior catalytic activity. By fitting the Nyquist plots to the equivalent circuit (inset in Figure S18), the R_{ct} of D-Fe-Ni$(OH)_2$ is estimated as merely 1.2 Ω, which is far less than that of β-Ni$(OH)_2$ (87 Ω) and NiFeOH-2 (2.6 Ω). EIS data support that the Fe doping in Ni$(OH)_2$ can significantly reduce the charge transfer resistance and the Ni foam scaffold is an effective conduction path, which leads to the outstanding catalytic activity of D-Fe-Ni$(OH)_2$.[29] D-Fe-Ni$(OH)_2$ maintains its OER activity for at least 10 h at 30 mA cm^{-2}, and its operational stability is confirmed with a continuous 500 CV cycles that show only a slight change (Figure 4D), which is more stable than pristine β-Ni$(OH)_2$ (Figure S19). The structural stability of D-Fe-Ni$(OH)_2$ was also evaluated by comparing its morphology and crystal structure before and after OER. As shown in Figure S20, the morphology and the XRD pattern of D-Fe-Ni$(OH)_2$ remain unchanged, indicating its stability during OER.

2.4 | OER catalytic mechanism of D-Fe-Ni$(OH)_2$

In situ Raman spectroscopy was engaged to gain insights into the catalytic mechanism by monitoring the surface species as applied potential varies in real-time. Figure 5A shows the Raman spectra of D-Fe-Ni$(OH)_2$ at open-circuit potential and an applied potential from 1.274 to 1.624 V. Initially in the air, two bands attributed to the Ni—O vibration in Ni$(OH)_2$ and disordered and/or Fe-doped Ni$(OH)_2$ are observed at 461 and 530 cm^{-1}, respectively.[30,31] Upon immersion in 1.0 M KOH electrolyte, the intensities of these bands greatly drop owing to the scattering effect of the electrolyte. At the applied potential of 1.374 V, a new band (peak ii) emerges at 560 cm^{-1}, which intensifies as the applied potential increases. At 1.424 V, another band (peak i) develops as a broad peak at 479 cm^{-1}. These peaks i and ii are ascribed to the Ni—O vibrations in NiOOH, and thus their growing intensities at higher potentials indicate a phase transformation from Ni$(OH)_2$ to NiOOH.[32] It is well known that NiOOH has two phases: β- and γ-NiOOH. Generally, β-NiOOH exhibits a higher peak ii intensity than peak i, that is, a higher intensity ratio of peak ii/peak i compared with γ-NiOOH.[33,34] Figure 5B discloses that the peak ii/peak i ratio increases with the increase in applied potential, which suggests the formation of β-NiOOH in
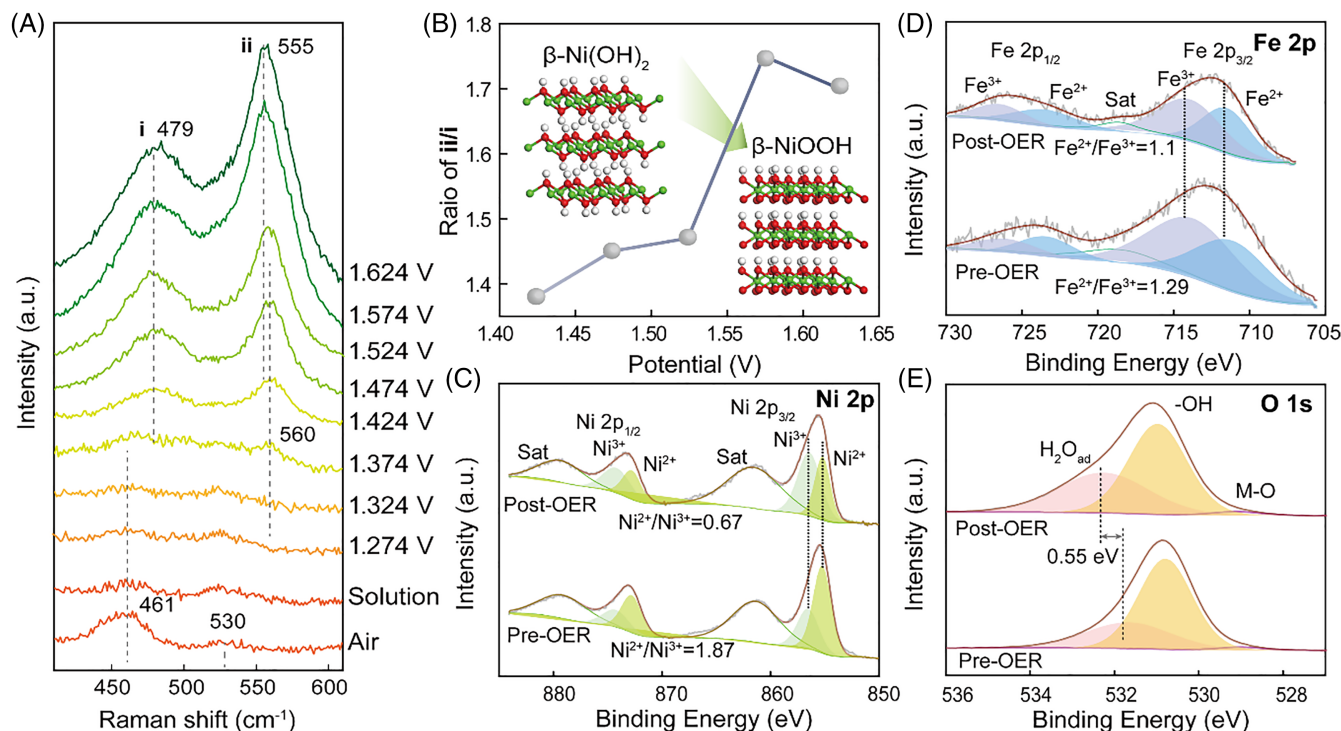
FIGURE 5 (A) In situ Raman spectra of D-Fe-Ni(OH)$_2$ collected as a function of applied potential (vs. reversible hydrogen electrode [RHE]) in 1.0 M KOH. Peaks i and ii are related to Ni–O vibrations in NiOOH. (B) The intensity ratio of peaks ii to i at various applied potentials. X-ray photoelectron spectroscopy (XPS) spectra of D-Fe-Ni(OH)$_2$ in (C) Ni 2p, (D) Fe 2p, and (E) O 1s regions before and after oxygen evolution reaction (OER) catalysis

D-Fe-Ni(OH)$_2$ during OER. This agrees well with the dominating β-Ni(OH)$_2$ phase, as revealed by a previous XRD characterization (Figure 1B), can be easily converted to β-NiOOH phase. At the potentials above 1.574 V, the peak ii shows an apparent red-shift to 555 cm^{-1}, which indicates the accumulation of Ni^{4+} species caused by the further oxidation of β-Ni^{3+}OOH to β-Ni^{4+}OOH.[35]

The surface chemical states of D-Fe-Ni(OH)$_2$ were investigated after OER by XPS (Figure 5C–E). The post-OER spectra in Ni 2p, Fe 2p, and O 1s regions exhibit only slight changes after OER, which indicates high stability of D-Fe—Ni(OH)$_2$ structure during the OER process. However, the Ni^{2+}/Ni^{3+} and Fe^{2+}/Fe^{3+} ratios drop from 1.87 to 0.67 and 1.29 to 1.10, respectively, which confirms the formation of high valent Ni^{3+} and Fe^{3+} species. This suggests that the active phase of D—Fe—Ni(OH)$_2$ is β-Ni^{3+}(Fe^{3+})OOH, and the Ni^{3+} species is further oxidized to Ni^{4+} species at a higher potential.[36] In the O 1s spectra, the H$_2$O$_{ad}$ peak is positively shifted by 0.55 eV with an intensity increase of 35% after OER. This indicates a strongly hydrophilic nature of active β-Ni^{3+}(Fe^{3+})OOH species, which allows full and intimate contact with electrolyte for a maximum active surface area.

3 | CONCLUSION

In summary, a series of D-Fe-Ni(OH)$_2$ was prepared by engaging BDPA organic ligands and modulating the amounts of Fe(NO$_3$)$_3$ during the hydrothermal synthesis. The BDPA plays a crucial role in achieving a high Fe doping level in β-Ni(OH)$_2$ by forming the Fe$_x$BDPA$_y$ precursors that induce a kinetically controlled metal ion exchange reaction with the Ni foam. The D-Fe-Ni(OH)$_2$ of ca. 9.9% Fe doping shows high OER activity with an ultralow overpotential of 194 mV at 10 mA cm^{-2}, outperforming most Ni(OH)$_2$-based electrocatalysts reported so far. The superb OER activity of D-Fe-Ni(OH)$_2$ is attributed to its transformation to the active species, amorphous β-Ni^{3+}Fe^{3+}OOH, with a low energy barrier benefiting from the unique structure.

4 | EXPERIMENTAL SECTION

4.1 | Chemicals and materials

Iron(III) nitrate nonahydrate (Fe(NO$_3$)$_3$·9H$_2$O, >97%), nitric acid (HNO$_3$, 69%), potassium hydroxide (KOH, ≥ 99%), and hydrochloric acid (HCl, 37%) were purchased

from Sigma–Aldrich. 1,4-Phenylenediphosphonic acid (BDPA, 97%) was obtained from TCI Inc. All chemicals were used as received. Nickel foam (thickness = 0.5 mm) was purchased from Shenzhen Teensky Technology Co. Ltd.

4.2 | Synthesis of disordered iron-doped nickel(II) hydroxide (D-Fe-Ni(OH)$_2$) on nickel foam

A piece of Ni form was cut (1.7 × 1.7 cm^2) and sonicated in 3 M HCl, acetone, and absolute ethanol in sequence for 10 min each. In a typical synthesis, the Ni foam was soaked in an aqueous solution (9 ml) containing BDPA (59.5 mg, 27.7 mM), and the solution was stirred for 10 min. Then, Fe(NO$_3$)$_3$ solution (1 ml, 0.75 M) was slowly added to this solution, followed by stirring for another 10 min. The reaction mixture was then heated to 180°C for 12 h in a 15 ml Teflon-lined stainless-steel autoclave. After the reaction, the product was collected as white precipitate, which was washed with deionized water and absolute ethanol repeatedly, and dried at 80°C under vacuum overnight.

4.3 | Materials characterizations

SEM was performed using a TESCAN VAGA3 (TESCAN, USA). TEM was conducted on a JEOL JEM-2100 F STEM at 200 kV using a holey carbon-coated 400 mesh Cu TEM grid for sample loading. Energy dispersive spectrometer (EDS) equipped in the STEM was used to determine the elemental composition of samples. High-resolution scanning TEM (STEM) images were taken with a TEM (Titan Themis G2 60–300, Thermo Fisher Scientific, United States) at 300 kV with a probe convergence angle of 17.8 mrad and a spatial resolution of 0.08 nm. The high-angle annular dark field (HAADF) images were acquired using an annular-type STEM detector with a collection inner semi-angle of 84 mrad, while bright field (BF)-STEM images were simultaneously recorded using a STEM BF detector. Electron energy loss spectroscopy (EELS) was performed with a Quantum 965 GIF system (Gatan Inc., United States), and the dual EELS were performed with a spectrometer dispersion chosen for simultaneous visualization of zero-loss O K-edge, Ni L edge, and Fe L-edge spectra. The energy resolution determined by the full-width at half-maximum of the zero-loss peak was ca. 1.1 eV. The background was subtracted using the power law method. XPS was carried out using a Thermo Fisher Nexsa with a monochromic Al Kα X-ray source

and pass energy of 1486.6 eV. Powder X-ray diffraction (XRD) patterns were recorded on a Rigaku SmartLab 9KW advance diffractometer with Cu Kα radiation (λ = 1.5406 Å) from 2θ = 5°–60° with a step increment of 0.01° at 3° min^{-1}. Raman spectroscopic measurements were performed on a Renishaw Micro-Raman Spectroscopy System by scanning from 100 to 2000 cm^{-1} with an excitation wavelength of 738 nm. Inductively coupled plasma optical emission spectrometry (ICP-OES, Agilent 710) was employed to determine the Fe doping content in the samples.

4.4 | Electrochemical measurements

All the electrochemical measurements were conducted using PARSTAT 2273 with a typical three-electrode configuration at room temperature. A graphite disk electrode and a Hg/HgO were used as the counter and reference electrodes, respectively, and 1 M potassium hydroxide (KOH) solution was used as the electrolyte unless otherwise specified. The as-synthesized samples were directly used as the working electrode. The recorded potential was referenced to a reversible hydrogen electrode (RHE) according to the following equation:

$$E\,(\mathrm{V\,vs.RHE}) = E\,(\mathrm{V\,vs.Hg/HgO}) + 0.098 + 0.059 \times \mathrm{pH}$$

Before each measurement, the working electrode was cycled between 0.2 and 0.8 V at 50 mV s^{-1} until stabilized. The OER performance was accessed by conducting LSV in an applied potential range between 0.2 and 0.8 V with a step size of 0.01 mV at a scan rate of 0.1 mV s^{-1} in an O$_2$-saturated electrolyte. The electrochemical double-layer capacitance (C_{dl}) was obtained by measuring CVs in a potential range of 0.2–0.3 V at various scan rates of 5, 10, 20, 40, 60, and 80 mV s^{-1} and used to calculate the ECSA of a catalyst. EIS was carried out by sweeping the frequency from 100 kHz to 0.1 Hz at the OER condition of 0.5 V. The collected EIS data were fit to the simplified Randles circuit to determine the charge transfer resistance.

AUTHOR CONTRIBUTIONS
Shuisheng Hu: Conceptualization, Data Curation, Formal Analysis, Writing – Original Draft Preparation. **Yong Li:** Conceptualization, Data Curation, Formal Analysis, Writing – Original Draft Preparation. **Daekyu Kim:** Data Curation, Formal Analysis. **Mengjie Liu:** Data Curation, Formal Analysis. **Lawrence Yoon Suk Lee:** Conceptualization, Funding Acquisition, Supervision, Writing – Review & Editing. **Kwok-Yin Wong:** Funding Acquisition, Supervision, Writing – Review & Editing.

CONFLICT OF INTEREST

The authors declare no conflict of interest.

ORCID

Lawrence Yoon Suk Lee https://orcid.org/0000-0002-6119-4780
Kwok-Yin Wong https://orcid.org/0000-0003-4984-7109

REFERENCES

1. Yu ZY, Duan Y, Feng XY, Yu X, Gao MR, Yu SH. Clean and affordable hydrogen fuel from alkaline water splitting: past, recent progress, and future prospects. _Adv Mater_. 2021;33(31):2007100.
2. Zhao X, Pachfule P, Li S, Simke JRJ, Schmidt J, Thomas A. Bifunctional electrocatalysts for overall water splitting from an iron/nickel-based bimetallic metal–organic framework/dicyandiamide composite. _Angew Chem Int Ed_. 2018;57(29):8921-8926.
3. Dionigi F, Zeng Z, Sinev I, et al. In-situ structure and catalytic mechanism of NiFe and CoFe layered double hydroxides during oxygen evolution. _Nat Commun_. 2020;11(1):2522.
4. Trotochaud L, Young SL, Ranney JK, Boettcher SW. Nickel–iron oxyhydroxide oxygen-evolution electrocatalysts: the role of intentional and incidental iron incorporation. _J Am Chem Soc_. 2014;136(18):6744-6753.
5. Chen JYC, Dang L, Liang H, et al. Operando analysis of NiFe and Fe oxyhydroxide electrocatalysts for water oxidation: detection of Fe^{4+} by Mössbauer spectroscopy. _J Am Chem Soc_. 2015;137(48):15090-15093.
6. Chen C, Zhang P, Wang M, et al. Boosting electrocatalytic water oxidation by creating defects and lattice-oxygen active sites on Ni-Fe nanosheets. _ChemSusChem_. 2020;3(18):5067-5072.
7. Mahala C, Devi Sharma M, Basu M. Fe-doped nickel hydroxide/nickel oxyhydroxide function as an efficient catalyst for the oxygen evolution reaction. _ChemElectroChem_. 2019;6(13):3488-3498.
8. Wu Y, Ji S, Wang H, Pollet BG, Wang X, Wang R. A highly efficient water electrolyser cell assembled by asymmetric array electrodes based on Co, Fe-doped $Ni(OH)_2$ nanosheets. _Appl Surf Sci_. 2020;528:146972.
9. Jiang J, Zhang A, Li L, Ai L. Nickel–cobalt layered double hydroxide nanosheets as high-performance electrocatalyst for oxygen evolution reaction. _J Power Sources_. 2015;278:445-451.
10. Kou T, Wang S, Hauser JL, et al. Ni foam-supported Fe-doped β-$Ni(OH)_2$ nanosheets show ultralow overpotential for oxygen evolution reaction. _ACS Energy Lett_. 2019;4(3):622-628.
11. Yin H, Jiang L, Liu P, et al. Remarkably enhanced water splitting activity of nickel foam due to simple immersion in a ferric nitrate solution. _Nano Res_. 2018;11(8):3959-3971.
12. Liu W, Yin R, Xu X, Zhang L, Shi W, Cao X. Structural engineering of low-dimensional metal–organic frameworks: synthesis, properties, and applications. _Adv Sci_. 2019;6(12):1802373.
13. Feng L, Wang K-Y, Powell J, Zhou H-C. Controllable synthesis of metal-organic frameworks and their hierarchical assemblies. _Matter_. 2019;1(4):801-824.
14. Zheng W, Liu M, Lee LYS. Electrochemical instability of metal–organic frameworks: _in situ_ spectroelectrochemical investigation of the real active sites. _ACS Catal_. 2020;10(1):81-92.
15. Huang J, Xu P, Cao D, et al. Asymmetric supercapacitors based on β-$Ni(OH)_2$ nanosheets and activated carbon with high energy density. _J Power Sources_. 2014;246:371-376.
16. Wang Y, Zhu Q, Zhang H. Fabrication of β-$Ni(OH)_2$ and NiO hollow spheres by a facile template-free process. _Chem Commun_. 2005;(41):5231-5233.
17. Hobbs C, Downing C, Jaskaniec S, Nicolosi V. TEM and EELS characterization of Ni–Fe layered double hydroxide decompositions caused by electron beam irradiation. _NPJ 2D Mater Appl_. 2021;5:1-9.
18. Zhou D, Jia Y, Duan X, et al. Breaking the symmetry: gradient in NiFe layered double hydroxide nanoarrays for efficient oxygen evolution. _Nano Energy_. 2019;60:661-666.
19. An L, Jiang N, Li B, et al. A highly active and durable iron/cobalt alloy catalyst encapsulated in N-doped graphitic carbon nanotubes for oxygen reduction reaction by a nanofibrous dicyandiamide template. _J Mater Chem A_. 2018;6(14):5962-5970.
20. Wan W, Wei S, Li J, Triana CA, Zhou Y, Patzke GR. Transition metal electrocatalysts encapsulated into N-doped carbon nanotubes on reduced graphene oxide nanosheets: efficient water splitting through synergistic effects. _J Mater Chem A_. 2019;7(25):15145-15155.
21. Li L, Yang X, Lei Y, et al. Ultrathin Fe-NiO nanosheets as catalytic charge reservoirs for a planar Mo-doped $BiVO_4$ photoanode. _Chem Sci_. 2018;9(47):8860-8870.
22. Su Y-Z, Xiao K, Li N, Liu Z-Q, Qiao S-Z. Amorphous $Ni(OH)_2$@three-dimensional Ni core–shell nanostructures for high capacitance pseudocapacitors and asymmetric supercapacitors. _J Mater Chem A_. 2014;2(34):13845-13853.
23. Yang H, Wang C, Zhang Y, Wang Q. Chemical valence-dependent electrocatalytic activity for oxygen evolution reaction: a case of nickel sulfides hybridized with N and S co-doped varbon nanoparticles. _Small_. 2018;14(8):1703273.
24. Jiang Y, Gao S, Xu G, Song X. Porous and amorphous cobalt hydroxysulfide core–shell nanoneedles on Ti-mesh as a bifunctional electrocatalyst for energy-efficient hydrogen production via urea electrolysis. _J Mater Chem A_. 2021;9(9):5664-5674.
25. Kang T, Wang Y, Guo F, et al. Self-assembled monolayer enables slurry-coating of Li anode. _ACS Cent Sci_. 2019;5(3):468-476.
26. Guo F, Kang T, Liu Z, et al. Advanced lithium metal–carbon nanotube composite anode for high-performance lithium–oxygen batteries. _Nano Lett_. 2019;19(9):6377-6384.
27. Li Y, Hu L, Zheng W, et al. Ni/co-based nanosheet arrays for efficient oxygen evolution reaction. _Nano Energy_. 2018;52:360-368.

28. Chen P, Xu K, Fang Z, et al. Metallic Co_4N porous nanowire arrays activated by surface oxidation as electrocatalysts for the oxygen evolution reaction. *Angew Chem Int Ed*. 2015;54(49): 14710-14714.

29. Zhu K, Liu H, Li M, et al. Atomic-scale topochemical preparation of crystalline Fe^{3+}-doped β-Ni(OH)$_2$ for an ultrahigh-rate oxygen evolution reaction. *J Mater Chem A*. 2017;5(17):7753-7758.

30. Louie MW, Bell AT. An investigation of thin-film Ni–Fe oxide catalysts for the electrochemical evolution of oxygen. *J Am Chem Soc*. 2013;135(33):12329-12337.

31. Zhou Y, Li Y, Zhang L, et al. Fe-leaching induced surface reconstruction of Ni-Fe alloy on N-doped carbon to boost oxygen evolution reaction. *Chem Eng J*. 2020;394:124977.

32. Jiang J, Sun F, Zhou S, et al. Atomic-level insight into super-efficient electrocatalytic oxygen evolution on iron and vanadium co-doped nickel (oxy)hydroxide. *Nat Commun*. 2018;9(1):2885.

33. Trześniewski BJ, Diaz-Morales O, Vermaas DA, et al. In situ observation of active oxygen species in Fe-containing Ni-based oxygen evolution catalysts: the effect of pH on electrochemical activity. *J Am Chem Soc*. 2015;137(48):15112-15121.

34. Yeo BS, Bell AT. In situ Raman study of nickel oxide and gold-supported nickel oxide catalysts for the electrochemical evolution of oxygen. *J Phys Chem C*. 2012;116(15):8394-8400.

35. Zheng X, Zhang B, De Luna P, et al. Theory-driven design of high-valence metal sites for water oxidation confirmed using in situ soft X-ray absorption. *Nat Chem*. 2018;10(2):149-154.

36. Su X, Wang Y, Zhou J, Gu S, Li J, Zhang S. Operando spectroscopic identification of active sites in NiFe Prussian blue analogues as electrocatalysts: activation of oxygen atoms for oxygen evolution reaction. *J Am Chem Soc*. 2018;140(36): 11286-11292.

SUPPORTING INFORMATION

Additional supporting information can be found online in the Supporting Information section at the end of this article.